J. Fluid Mech. (2019), *vol.* 875, R1, doi:10.1017/jfm.2019.540

JFM RAPIDS
journals.cambridge.org/rapids

Swimming freely near the ground leads to flow-mediated equilibrium altitudes

Melike Kurt[1],†, Jackson Cochran-Carney[1], Qiang Zhong[2], Amin Mivehchi[1], Daniel B. Quinn[2] and Keith W. Moored[1]

[1]Department of Mechanical Engineering, Lehigh University, Bethlehem, PA 18015, USA

[2]Department of Aerospace and Mechanical Engineering, University of Virginia, Charlottesville, VA 22904, USA

(Received 29 April 2019; revised 28 June 2019; accepted 28 June 2019; first published online 18 July 2019)

Experiments and computations are presented for a foil pitching about its leading edge near a planar, solid boundary. The foil is examined when it is constrained in space and when it is unconstrained or freely swimming in the cross-stream direction. It was found that the foil has stable equilibrium altitudes: the time-averaged lift is zero at certain altitudes and acts to return the foil to these equilibria. These stable equilibrium altitudes exist for both constrained and freely swimming foils and are independent of the initial conditions of the foil. In all cases, the equilibrium altitudes move farther from the ground when the Strouhal number is increased or the reduced frequency is decreased. Potential flow simulations predict the equilibrium altitudes to within 3 %–11 %, indicating that the equilibrium altitudes are primarily due to inviscid mechanisms. In fact, it is determined that stable equilibrium altitudes arise from an interplay among three time-averaged forces: a negative jet deflection circulatory force, a positive quasistatic circulatory force and a negative added mass force. At equilibrium, the foil exhibits a deflected wake and experiences a thrust enhancement of 4 %–17 % with no penalty in efficiency as compared to a pitching foil far from the ground. These newfound lateral stability characteristics suggest that unsteady ground effect may play a role in the control strategies of near-boundary fish and fish-inspired robots.

Key words: flow–structure interactions, propulsion, swimming/flying

1. Introduction

Airfoils have long been known to have reduced downwash and high lift-to-drag ratios near the ground (Cui & Zhang 2010). This ‘steady ground effect’ has inspired the design of several wing-in-ground effect aircraft (Rozhdestvensky 2006). In nature,

† Email address for correspondence: mek514@lehigh.edu

animals such as birds and flying fish use steady ground effect to improve their cost of transport or gliding distance (Hainsworth 1988; Rayner 1991; Park & Choi 2010). In contrast, some fish exploit unsteady ground effect to improve their cost of transport or cruising speed when swimming near substrates and sidewalls (Blake 1983; Webb 1993, 2002; Nowroozi *et al.* 2009; Blevins & Lauder 2013), and it is important in the take-off and landing of insects (Van Truong *et al.* 2013*a*,*b*). In unsteady ground effect, fin/wing/tail/body oscillations create time-dependent wakes and continuous fluctuations in the pressure field. Unsteady ground effect differs from steady ground effect in that it produces thrust enhancement, a ubiquitous deflection of wake momentum away from the ground, and negative lift regimes at moderate ground proximities on the order of a chord length (Quinn *et al.* 2014*b*).

Unsteady ground effect was first examined through the development of analytical models for a fluttering plate in a channel (Tanida 2001) and for an oscillating wing in weak ground effect (Iosilevskii 2008), but these only apply in extreme cases, such as flying/swimming very far from or very close to the ground. At more moderate ground proximities, experiments and computations have shown that rigid (Quinn *et al.* 2014*b*; Mivehchi, Dahl & Licht 2016; Perkins *et al.* 2018) and flexible (Blevins & Lauder 2013; Quinn, Lauder & Smits 2014*a*; Fernández-Prats *et al.* 2015; Dai, He & Zhang 2016; Park, Kim & Sung 2017; Zhang, Huang & Lu 2017) oscillating foils and wings can have improved thrust production with little or no penalty in efficiency when operating in unsteady ground effect. Additionally, Quinn *et al.* (2014*b*) found both negative and positive time-averaged lift regimes for constrained (as opposed to freely swimming) pitching foils near the ground. They hypothesized that a freely swimming pitching foil would settle into an equilibrium altitude as fluid-mediated forces pushed the foil to the edge of these lift regimes. This surprising result was shown for a constrained foil within a potential flow numerical framework (Quinn *et al.* 2014*b*), leaving open questions as to whether viscosity and/or recoil motions would disrupt the existence of these equilibrium altitudes. Recent tow tank experiments provided more evidence for equilibrium altitudes by finding negative and positive lift zones for constrained, near-ground, heaving and pitching foils (Mivehchi *et al.* 2016). Recent low-Reynolds-number ($Re = 100$) computations of near-ground, flexible, freely swimming plates also found equilibrium altitudes, but could not test whether the altitudes persist at high Reynolds numbers (Kim *et al.* 2017). No previous work has experimentally confirmed the equilibrium altitudes for freely swimming foils, nor is it known whether the equilibrium altitudes are affected by swimming kinematics.

Motivated by these observations, we present new experiments and computations aimed at probing the existence of equilibrium altitudes and their dependence upon non-dimensional variables for high-Reynolds-number swimmers operating in unsteady ground effect. We consider two pitching foil systems: one constrained to fixed positions and another unconstrained and free to move in the cross-stream direction. Two main questions are considered: do equilibrium altitudes exist for an oscillating foil in the presence of a solid boundary, and if so, how are they affected by swimming variables such as the Strouhal number and reduced frequency?

2. Methods

The hydrofoil used throughout this study has a rectangular-planform shape, a 7 % thick tear-drop cross-section (Godoy-Diana, Aider & Wesfreid 2008; Quinn *et al.* 2014*b*), and a chord and span length of $c = 0.095$ m and $s = 0.19$ m ($\mathcal{AR} = 2$), respectively. It was fabricated out of acrylonitrile butadiene styrene (ABS).

	Constrained experiments	Unconstrained experiments/simulations
A^*	0.125, 0.25, 0.38, 0.49, 0.61	0.15, 0.2, 0.25, 0.3
D^*	0.25–2.6	—
D_0^*	—	0.25, 0.5, 0.75
St	0.06–0.63	0.3, 0.4, 0.5
k	0.52, 0.77, 1.02	0.5, 0.75, 1

TABLE 1. Experimental and numerical variables used in the constrained and unconstrained foil experiments, and the unconstrained simulations.

The hydrofoil was actuated with pure pitching motion about its leading edge by a digital servo motor (constrained experiments: Dynamixel MX-64AT, unconstrained experiments: Dynamixel MX-64), and the angular position was tracked by an optical encoder (constrained experiments: US Digital E5, unconstrained experiments: US Digital A2K 4096 CPR). The prescribed sinusoidal motion can be defined as $\theta(t) = \theta_0 \sin(2\pi ft)$, where f is the frequency of the motion, t is the time and θ_0 is the pitching amplitude. Measurements were taken throughout this study at three flapping frequencies: $f = 0.5$, 0.75 and 1 Hz. The frequency is also used to defined the reduced frequency, $k \equiv fc/U$, and the Strouhal number, $St \equiv fA/U$. Here A is the peak-to-peak amplitude of motion – that is, $A = 2c \sin\theta_0$. The amplitude of motion is reported in its non-dimensional form as $A^* = A/c$. One of the primary variables of the current study is the non-dimensional ground distance, $D^* = D/c$, where D is the distance from the ground plane. Throughout the current study, the flow speed, U, was kept at 0.093 m s^{-1}, giving a chord-based Reynolds number of 9950. The input variables used are summarized in table 1.

For the constrained experiments and the simulations, the force production is measured and reported as the time-averaged thrust, $\overline{T}$, lift, $\overline{L}$, and power, $\overline{P}$, normalized by the dynamic pressure and planform area:

$$C_T \equiv \frac{\overline{T}}{\frac{1}{2}\rho U^2 cs}, \quad C_L \equiv \frac{\overline{L}}{\frac{1}{2}\rho U^2 cs}, \quad C_P \equiv \frac{\overline{P}}{\frac{1}{2}\rho U^3 cs}, \quad \eta \equiv \frac{C_T}{C_P}, \tag{2.1a–d}$$

where ρ is the density of the fluid medium and η is the propulsive efficiency. Here, the time-averaged power from the simulations is the time average of the pitching moment and the angular rate – that is, $\overline{P} = \overline{M_\theta \dot{\theta}}$.

2.1. *Constrained foil experiments*

Constrained foil experiments were conducted in a closed-loop water channel with a test section of 4.9 m long, 0.93 m wide and 0.61 m deep. In order to produce a nominally two-dimensional flow, a splitter and surface plate were installed near each hydrofoil tip (see figure 1*a*). A vertical ground wall was also installed on the side of the channel, as shown in figure 1(*a*). Five different non-dimensional amplitudes were tested: $A^* = 0.125$, 0.25, 0.38, 0.49 and 0.61. The non-dimensional ground distance was varied within the range $0.25 \leqslant D^* \leqslant 2.6$. Lift measurements were conducted with a six-axis force sensor (ATI Nano43). The lift data were time-averaged over 100 oscillation cycles, and each reported data point is the mean value of five trials.

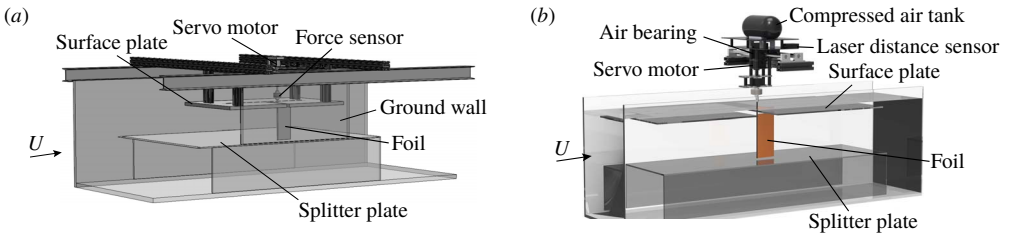

FIGURE 1. Schematic of the (*a*) constrained pitching hydrofoil set-up and (*b*) unconstrained hydrofoil set-up.

2.2. *Foil experiments unconstrained in the cross-stream direction*

Tests were also conducted for a pitching hydrofoil that was unconstrained in the cross-stream direction. The unconstrained hydrofoil was in a closed-loop water channel with a test section of 1.52 m long, 0.38 m wide and 0.45 m deep (Rolling Hills 1520). The hydrofoil was suspended from three air bushings (New Way S301901), giving it near-frictionless cross-stream freedom while constraining it in the streamwise direction (figure 1*b*). The compressed air was stored in a 4500 psi tank that moved with the hydrofoil, and the airflow was controlled by a programmable solenoid valve. A nominally two-dimensional flow was achieved by installing a horizontal splitter plate and a surface plate near the tips of the hydrofoil (figure 1*b*). The gap between the hydrofoil tips and the surface/splitter plate was less than 5 mm. Surface waves were also minimized by the presence of the surface plate.

The wall of the channel was used as a ground plane, and the ground distance was recorded by a laser distance sensor (Baumer CH-8501). The hydrofoil was placed at three initial positions: $D_0^* = 0.25$, 0.5 and 0.75. Each trial included at least 80 oscillation cycles. To eliminate any drag caused by cables, all angular position and laser sensor data were synchronized by a custom circuit and transmitted to a control PC (Omen 870) via wifi (ATI Wireless F/T).

2.3. *Foil simulations unconstrained in the cross-stream direction*

Potential flow simulations were employed to exactly match the foil experiments unconstrained in the cross-stream direction since previous potential flow numerical solutions for the constrained foil case have been reported (Quinn *et al.* 2014*b*). The matching of the experiments and simulations provides a direct means of assessing the role of viscosity. To model the flow over a foil unconstrained in the cross-stream direction, we used a two-dimensional boundary element method (BEM) based on potential flow theory in which the flow is assumed to be irrotational, incompressible and inviscid. By following previous studies (Katz & Plotkin 2001; Quinn *et al.* 2014*b*; Moored 2018), the general solution to the potential flow problem is reduced to finding a distribution of sources and doublets on the foil surface and in its wake. At each time step a no-flux boundary condition is enforced on the body.

To solve this problem numerically, constant-strength source and doublet line elements are distributed over the body and the wake. Each body element is assigned a collocation point, which is located at the centre of each element and shifted 1 % of local thickness into the body, where a constant-potential condition is applied to enforce no flux through the surface (i.e. Dirichlet formulation). This results in a matrix representation of the boundary condition that can be solved for the body

doublet strengths once a wake shedding model is applied. Additionally, at each time step, a wake boundary element is shed with a strength that is set by applying an explicit Kutta condition, where the vorticity at the trailing edge is set to zero (Willis 2006; Wie, Lee & Lee 2009; Pan *et al.* 2012). A wake roll-up algorithm is implemented at each time step where the wake elements are advected with the local velocity. During wake roll-up, the point vortices, representing the ends of the wake doublet elements, must be desingularized for numerical stability of the solution (Krasny 1986). At a cutoff radius of $\epsilon/c = 5 \times 10^{-2}$, the irrotational induced velocities from the point vortices are replaced with a rotational Rankine core model. The tangential perturbation velocity component is calculated by local differentiation of the perturbation potential. The pressure acting on the body is found via applying the unsteady Bernoulli equation. Moreover, the mean thrust force is calculated as the time average of the streamwise-directed pressure forces, and the time-averaged power input to the fluid is calculated as the time average of the negative inner product of the force vector and velocity vector of each boundary element – that is, $P = -\int_{\mathcal{S}} \boldsymbol{F}_{ele} \cdot \boldsymbol{u}_{ele} \, \mathrm{d}\mathcal{S}$, where $\mathcal{S}$ is the body surface.

The presence of the ground is modelled using the method of images, which automatically satisfies the no-flux boundary condition on the ground plane. The foil is also given a mass, m, equal to the effective mass of the moving portion of the apparatus in the unconstrained foil experiments, and is non-dimensionalized by the characteristic added mass of the hydrofoil as $m^* = m/(\rho s c^2) = 2.68$. At each time step the equation of motion in the cross-flow direction is solved through a one-way explicit coupling between the fluid flow and the body dynamics to calculate the location and velocity of the leading edge of the foil. For more details on the numerical method see Moored (2018) and Moored & Quinn (2018).

Convergence studies found that the equilibrium altitude changes by less than 2 % when the number of body panels, $N_b = 250$, and the number of time steps per cycle, $N_t = 250$, were doubled independently. The current study only considered the foil's cycle-averaged altitude $\overline{D^*}$ as a convergence metric, since this is the prime output variable of interest. The computations were run over 100 flapping cycles and the time-averaged data are obtained by averaging over the last 5 cycles. For all simulations there was less then 2 % change in the equilibrium altitude after 60 flapping cycles, except for the case of $(St, k) = (0.5, 1)$, which converged after 80 flapping cycles.

3. Results

3.1. *Stable equilibrium altitudes, performance and flow structures*

Figure 2(*a*) presents the lift coefficient measured from the constrained foil experiments at $k = 1.02$ as a function of the ground distance and Strouhal number. Far from the ground ($D^* \gtrsim 1$) there is negative time-averaged lift that acts to pull the foil towards the ground. Close to the ground ($D^* \lesssim 1$) the foil produces positive lift that acts to push the foil away from the ground. At a ground distance between these two lift regimes, the time-averaged lift is zero. These zero-lift ground distances represent stable equilibrium altitudes, D^*_{eq}. If a foil is perturbed away from or towards the ground, lift forces would act to return the foil to the equilibrium altitude. Additionally, with increasing Strouhal number, the minimum and maximum lift force is amplified and the equilibrium altitude moves farther from the ground. These constrained foil experiments confirm the potential flow results presented by Quinn *et al.* (2014*b*) and the existence of equilibrium altitudes shown by Mivehchi *et al.* (2016).

The equilibrium altitudes are determined by interpolating the lift data near the zero-lift ground distance with a cubic-spline function for each $St - k$ case listed in table 1

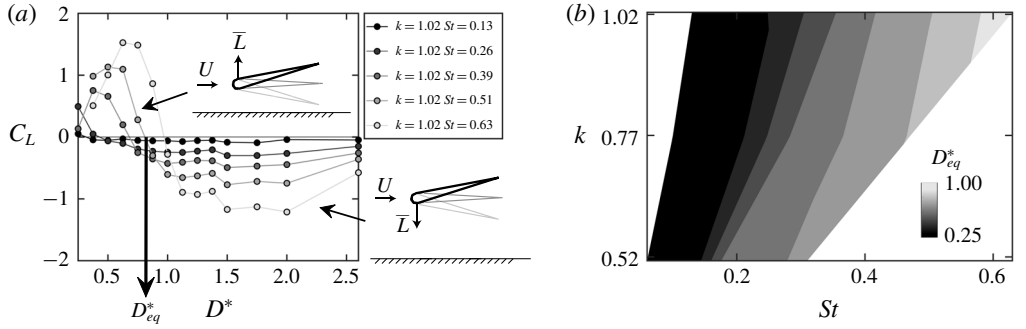

FIGURE 2. Constrained foil experiments: (*a*) lift coefficient as a function of the non-dimensional distance from the ground for $k = 1.02$ and (*b*) equilibrium altitude as a function of the Strouhal number and reduced frequency. No data are shown in the regions coloured with white.

for the constrained foil experiments. Figure 2(*b*) presents these equilibrium altitudes as a function of the Strouhal number and reduced frequency. Indeed, the equilibrium altitudes move farther from the ground as the Strouhal number increases for all of the reduced frequencies examined. In contrast, the equilibrium altitudes move closer to the ground as the reduced frequency increases.

The constrained foil experiments suggest that equilibrium altitudes exist for unsteady ground effect swimmers, but they cannot prove whether or not dynamic recoil motions of a freely swimming body alter the physics that give rise to these altitudes. To prove the existence of equilibrium altitudes for freely swimming foils, we tested foils that were free to move in the cross-stream direction. Figure 3 presents the foil's time-varying ground distance for $St = 0.3$ and various reduced frequencies measured from the experiments and simulations. Regardless of the initial condition and the reduced frequency, the foil reaches an equilibrium altitude in both the experiments and the simulations. Moreover, the equilibrium altitudes measured from the experiments and predicted by the simulations are in excellent agreement (<0.03 disagreement in D_{eq}). This agreement indicates that the physics of unsteady ground effect are dominated by inviscid phenomena. Additionally, the equilibrium altitude can be observed to move closer to the wall as the reduced frequency is increased, which is in agreement with the constrained foil experiments (figure 2*b*). The foil's trajectory shows sinusoidal recoil oscillations in the cross-stream direction with each pitching cycle. The amplitude of these oscillations are slightly higher in the numerical results than the experimental measurements (on the order of 10 %–20 %). This can be attributed to viscous flow effects such as mild separation and/or end effects in the experiments that are not present in the simulations, which can lead to increased experimental damping. The recoil oscillations can be observed to grow with decreasing reduced frequency, which can be explained by the increased pitching amplitude that occurs to maintain the Strouhal and Reynolds numbers among these cases.

Figure 4 presents the foil's time-varying ground distance for $k = 1$ and various Strouhal numbers measured from the experiments and simulations. Again, regardless of the initial condition, the foil converges to the same equilibrium altitude for all of the examined Strouhal numbers, and there is excellent agreement between numerics and experiments (<0.07 disagreement in D_{eq}). In fact, the numerically predicted

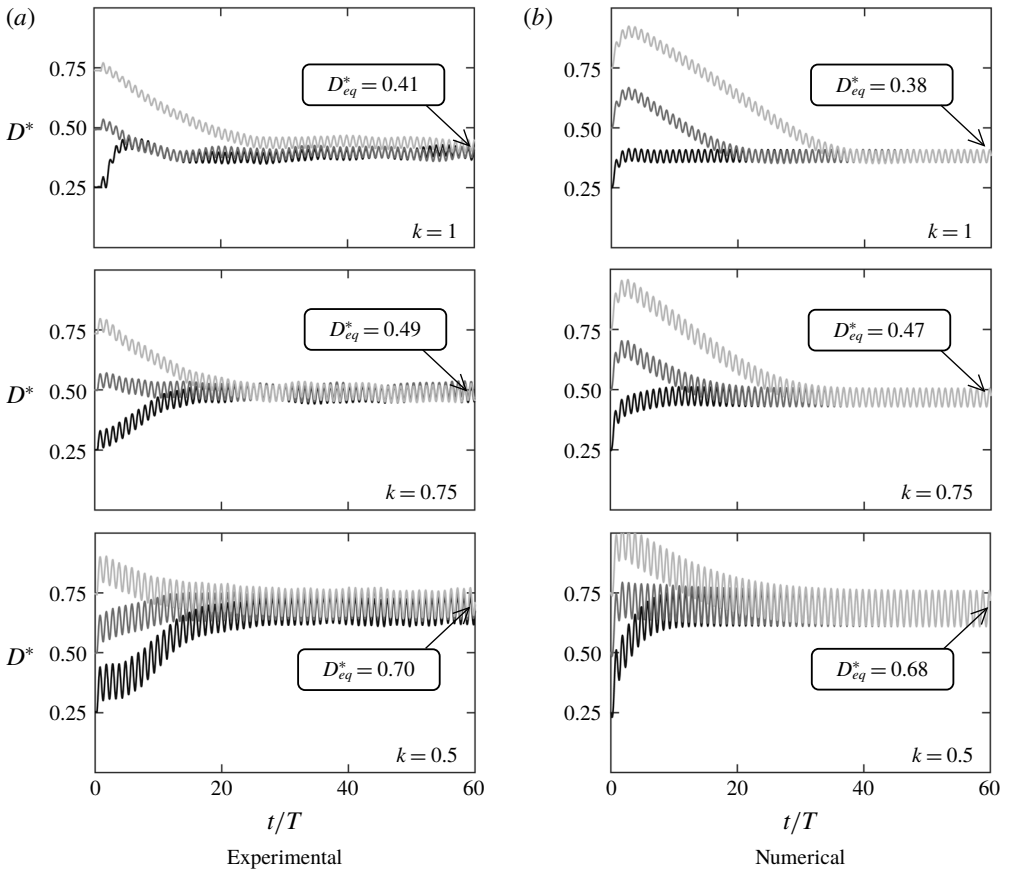

FIGURE 3. Time-varying ground distance as a function of time normalized by the period of motion, T, for $St = 0.3$. Data from (a) experiments and (b) simulations. The line colour from black to light grey represents three different initial conditions: $D^* = 0.25$, 0.5 and 0.75. Three reduced frequency cases of $k = 0.5$, 0.75 and 1 are presented.

equilibrium altitudes are within 3 %–11 % of the experimental measurements for all of the cases examined in figures 3 and 4. As the Strouhal number increases, recoil oscillations increase and the equilibrium altitudes move further away from the ground, in agreement with the constrained foil experiments (figure 2*b*). There is some disagreement between the simulations and experiments in the initial time-varying trajectories of the foil before an equilibrium altitude is reached. These discrepancies can be attributed to the same viscous flow effects highlighted before – that is, mild separation and/or end effects in the experiments that are not present in the simulations.

The potential flow simulations can be used to gain further insight into the energetic performance of the foils at the equilibrium altitudes. Table 2 presents the thrust, power, and propulsive efficiency for the unconstrained foils as compared to their values far from the ground. In agreement with previous findings (Quinn *et al.* 2014*b*), near-ground altitudes lead to improvements in thrust production with no penalty in efficiency. In fact, the thrust increases slightly more than the power (4 %–17 % versus 3 %–15 %), causing the efficiency to increase slightly (1 %–2 %). Freely swimming foils therefore automatically converge to altitudes where the same

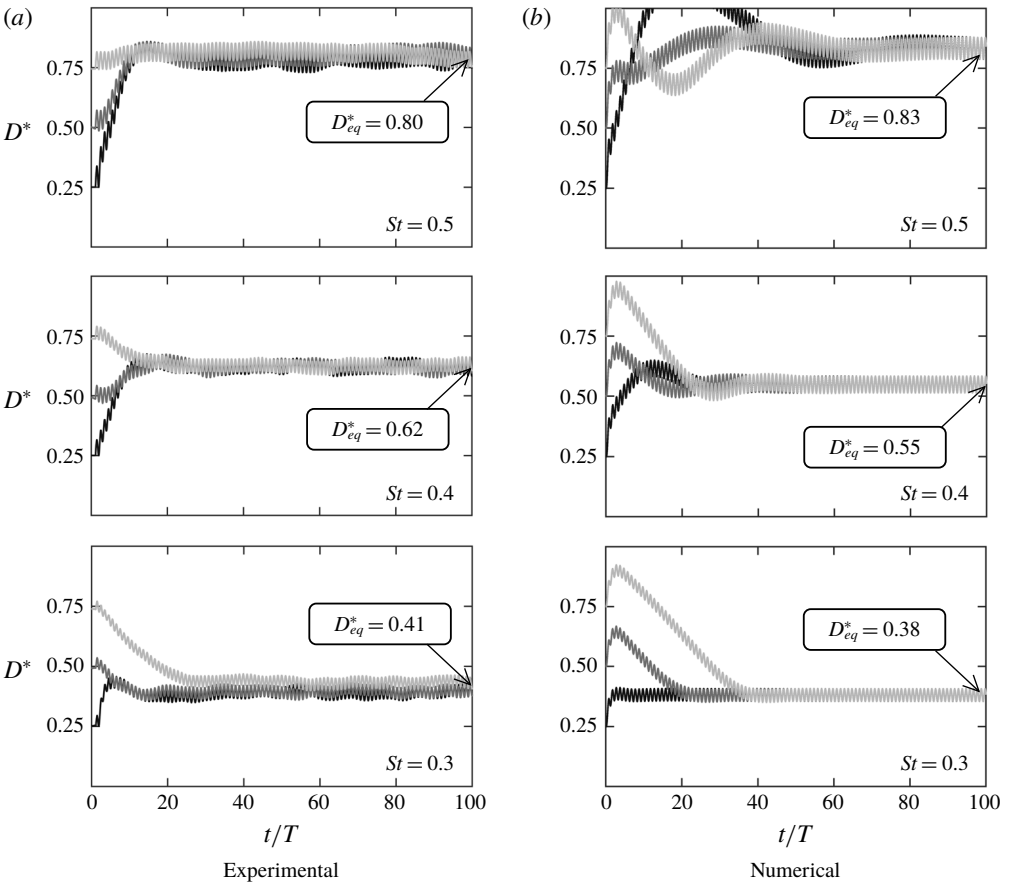

FIGURE 4. Time-varying ground distance as a function of normalized time for $k = 1$. Data from (*a*) experiments and (*b*) simulations. The line colour from black to light grey represents three different initial conditions: $D^* = 0.25$, 0.5 and 0.75. Three Strouhal number cases of $St = 0.3$, 0.4 and 0.5 are presented.

kinematics produce higher thrust. Regardless of St and k, the thrust improvement was found to monotonically increase as the equilibrium altitude decreased (table 2). However, the thrust improvements observed in the current study are smaller than those of previous findings (Quinn *et al.* 2014*b*). This is likely due to the recoil oscillations of the freely swimming foil in the current work. These lead to combined heaving and pitching motions that are out of phase, producing poor thrust performance.

Figure 5 presents flow fields generated by the simulations for the corresponding Strouhal number and reduced frequency cases. Regardless of the case examined, there is a ubiquitous wake deflection, as observed in previous work, that has been linked to inviscid vortex dynamics between the shed vortices and their images (Quinn *et al.* 2014*b*). It can also be observed that as the Strouhal number increases at constant reduced frequency ($k = 1$), the vortex spacing increases in the cross-stream direction as expected, since the amplitude of motion is increased. In contrast, as the reduced frequency increases at a fixed Strouhal number ($St = 0.3$) the wake vortices are compressed in the cross-stream and streamwise directions. This occurs since the

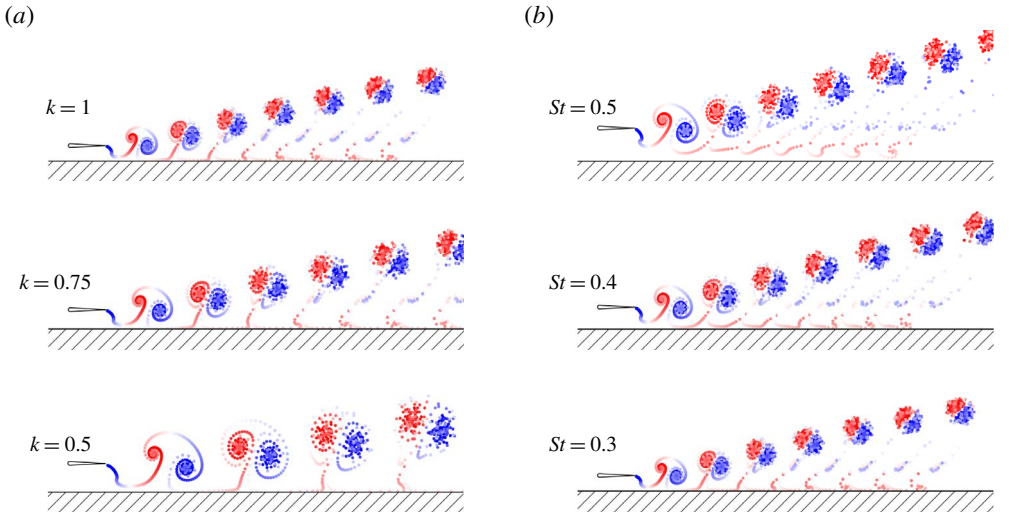

FIGURE 5. Simulated wake structures at (*a*) $St = 0.3$ for varying reduced frequency and (*b*) $k = 1$ for varying Strouhal number. Red and blue vortices represent counterclockwise and clockwise rotations, respectively.

	St	k	C_T^*	C_P^*	η^*	$D_{eq,num}^*$
Case 0	0.2	0.5	1.12	1.11	1.01	0.48
Case 1	0.3	0.5	1.08	1.06	1.01	0.68
Case 2	0.3	0.75	1.13	1.11	1.02	0.47
Case 3	0.3	1.0	1.17	1.15	1.02	0.38
Case 4	0.4	1.0	1.10	1.08	1.02	0.55
Case 5	0.5	1.0	1.04	1.03	1.01	0.83

TABLE 2. Thrust and power coefficients, and efficiency for the unconstrained foil simulations at steady-state equilibrium altitudes. The performance metrics are normalized by the corresponding value for a foil operating far from the ground and denoted with a superscript, $(.)^*$. Note that the trajectories for Case 0 are not shown in figures 3 and 4.

amplitude and vortex wavelength are reduced as the reduced frequency increases for a fixed Strouhal number and flow speed.

3.2. *Physical mechanisms leading to stable equilibrium altitudes*

We hypothesize that equilibrium altitudes arise from the balance among three effects (figure 6*a*): a negative circulatory lift force due to a deflected jet mechanism, a positive circulatory lift force due to a quasistatic mechanism, and a negative lift force due to an added mass mechanism. To investigate this hypothesis, we performed constrained pitching foil simulations with $St = 0.3$ and $k = 1$ over a range of dimensionless ground proximities ($0.22 \leqslant D^* \leqslant 1$). In the constrained foil simulations, the equilibrium altitude occurs at $D^* = 0.47$, which is further from the ground than in the unconstrained simulations of Case 3 reported in table 2. This is due to the difference in m^*, where $m^* = 2.68$ in the unconstrained simulations and $m^* = \infty$ in the constrained simulations, leading to combined heaving and pitching motion in

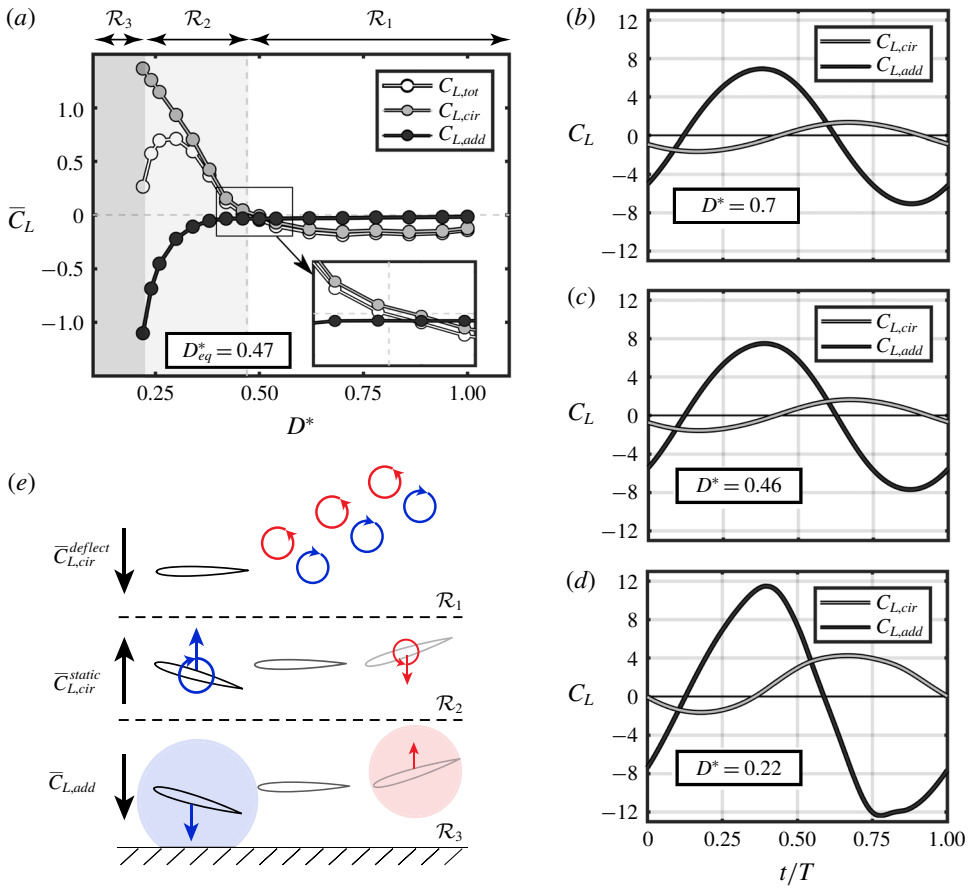

FIGURE 6. The decomposition of the lift force acting on a constrained pitching foil at various ground proximities. White, grey and black lines denote the total lift, circulatory lift and the added mass lift, respectively. (*a*) The cycle-averaged lift coefficient as a function of dimensionless ground proximity. The equilibrium altitude is located at $D^*_{eq} = 0.47$. The time-varying lift over a cycle at (*b*) $D^* = 0.70$, (*c*) $D^* = 0.46$ and (*d*) $D^* = 0.22$. (*e*) Schematic of the physical origins of the dominant lift forces in three regions ($\mathcal{R}_1$, $\mathcal{R}_2$ and $\mathcal{R}_3$).

the former and pure pitching motion in the latter. The boundary element simulations are used to decompose the computed lift force into its circulatory and added mass components. The instantaneous bound circulation of the foil is simply the negative of the strength of the trailing-edge element – that is, $\Gamma_{bound} = -\mu_{TE}$. The Kutta–Joukowski theorem is then used to the compute the circulatory lift coefficient. The added mass lift coefficient is the difference between the total lift coefficient and the circulatory lift coefficient.

The time-varying circulatory and added mass lift coefficients are presented in figure 6(*b–d*) for three ground proximities. Figure 6(*b*) shows a ground proximity that is above its equilibrium altitude at $D^* = 0.7$. The instantaneous added mass lift is nearly symmetric about the origin, leading to zero lift in the time average. In contrast, the magnitude of the trough in circulatory lift is slightly greater than the magnitude of the peak in circulatory lift, leading to a negative lift force in the time average due

to the deflected jet. Indeed, the time-averaged forces presented in figure 6(*a*) have a negligible time-averaged added mass force and a negative time-averaged circulatory force in the range $0.5 \leqslant D^* \leqslant 1$ in region $\mathcal{R}_1$, which supports the hypothesis of the jet deflection mechanism. Figure 6(*c*) shows a ground proximity that is slightly below the equilibrium altitude at $D^* = 0.46$. Both the instantaneous added mass and circulatory lift seem to be symmetric, although in the time average (figure 6*a*) the circulatory and added mass forces are slightly positive and negative, respectively. This highlights the fact that, in general, all three mechanisms balance to define an equilibrium altitude. However, below the equilibrium altitude in region $\mathcal{R}_2$ the time-averaged quasistatic circulatory force dominates the mechanisms, leading to a net positive lift force in the range $0.22 \leqslant D^* \leqslant 0.5$ (figure 6*a*). Figure 6(*d*) presents a ground proximity well below the equilibrium altitude at $D^* = 0.22$. Here the asymmetry in the added mass lift is clear, both in a difference in the magnitudes of the peak and trough and in the waveform of the signal, which leads to a time-averaged negative lift as hypothesized. The difference in the magnitude of the peak and trough of the circulatory force is also clear, highlighting the hypothesized quasistatic mechanism. Based on the rate of change of the time-averaged circulatory and added mass forces as a $D^* = 0.22$ is approached (figure 6*a*), we postulate that the negative added mass force will dominate the mechanisms for $D^* < 0.22$, leading to a net negative lift force in region $\mathcal{R}_3$ and an unstable equilibrium altitude between regions $\mathcal{R}_2$ and $\mathcal{R}_3$. Future work will examine this in more detail.

For all of the cases examined in this study, a deflected vortex wake has been observed, which in the time average forms a deflected jet away from the ground. When the foil is sufficiently far from the ground, one can imagine performing a control volume analysis on the time-averaged flow field to determine the net lift force. The sides of a rectangular control volume that are normal to the cross-stream direction can extend far enough from the foil such that the pressure on those boundaries would be of equal magnitude and act in opposite directions, leading to no net pressure force. The lift force would then solely arise from the rate of change of momentum due to the deflected jet, and it would act towards the ground ($\mathcal{R}_1$ in figure 6*e*). Given the ubiquitous deflected jet, it is expected that this negative lift force occurs at all of the ground proximities examined, and it can be understood as an unsteady circulatory force. The deflected jet disappears as the wake strength disappears with decreasing reduced frequency and as the foil is moved far from the ground. It is expected that the magnitude of the negative lift force from the deflected jet would then scale with increasing k and inversely with D^*.

At moderate ground proximities, the control volume's lower boundary must coincide with the ground plane in order to be as far from the foil as possible without additional ground reaction forces arising from the control volume cutting through the ground itself. However, at moderate distances from the ground, the pressure on the ground will not be at the free-stream pressure, and a net pressure force acting on the control volume away from the ground (pressure elevated above the free stream on the ground) will arise. Fundamentally, this will give rise to a net positive bound circulation in the time average. This can be further understood as a quasistatic circulatory force, also known as the classical steady ground effect. When the foil reaches the bottom of its downstroke, it will be closer to the ground than when it reaches the top of its upstroke, leading to a greater enhancement of the bound circulation at the closest proximity position and a time-averaged positive lift force ($\mathcal{R}_2$ in figure 6*e*). Since the magnitude of this force depends on the difference in bound circulation enhancement at the foil's extreme positions, it is expected that this quasistatic force will increase with increasing amplitude of motion.

At close ground proximities, a time-averaged added mass lift force arises that cannot be understood through a steady control volume analysis. Classic theory describes that the added mass of a cylinder near a ground plane should increase inversely with the dimensionless ground proximity squared (Keulegan 1958; Brennen 1982). Therefore, when the foil reaches the bottom of its downstroke its added mass will be amplified more than when the foil is at the top of its upstroke. At the bottom of its downstroke, the foil experiences a negative added mass lift force, which would then be larger in magnitude than the positive added mass lift force experienced at the top of its upstroke. This imbalance will lead to a negative time-averaged added mass lift force ($\mathcal{R}_3$ in figure 6*e*). Since the magnitude of this force also depends on the difference in the extreme positions, it is expected that it will increase with increasing amplitude of motion.

Now the mechanisms behind the observed trends in the equilibrium altitude with variations in St and k can be postulated. In the current study, St is increased by increasing the amplitude of motion. This should increase the magnitude of the quasistatic circulatory force and the added mass force, thereby pushing the equilibrium altitude (the boundary between regions $\mathcal{R}_1$ and $\mathcal{R}_2$) further from the ground. When the reduced frequency is increased, the magnitude of the jet deflection force should increase, thereby pushing the equilibrium altitude closer to the ground. Alternatively, when the reduced frequency is increased the amplitude of motion is also decreased, which consequently will weaken the quasistatic and added mass forces, thereby moving the equilibrium closer to the ground as well.

4. Conclusions

For the first time, it is experimentally confirmed that freely swimming pitching foils converge to stable equilibrium altitudes. When the foils are within approximately 1–3 chord lengths of the ground, negative lift forces pull them towards the ground; when the foils are closer than approximately 1 chord to the ground, positive lift forces push them away from the ground. These equilibrium altitudes are insensitive to initial altitude. Furthermore, the equilibria are dependent on swimming kinematics: in both constrained and unconstrained cases, equilibrium altitudes increase with increasing Strouhal number and decreasing reduced frequency. Despite viscous boundary layers on the foil and the ground in the experiments, there is excellent agreement between the potential flow simulations and the experiments for all of the cases considered (3 %–11 % difference). This suggests that the equilibrium altitudes are primarily an inviscid phenomenon. The physical mechanisms leading to stable equilibrium altitudes were identified as an interplay among three time-averaged forces: a negative jet deflection circulatory force, a positive quasistatic circulatory force and a negative added mass force.

The existence of equilibrium altitudes has significant implications for near-ground swimming. Swimming outside of equilibrium could incur an energetic penalty, because doing so would require asymmetric motions to counteract near-ground lift forces. Over the range of conditions considered, swimming at equilibrium led to higher thrusts and efficiencies (4 %–17 % and 1 %–2 % higher than far from the ground, respectively). However, thrust increases as high as 44 % have been observed closer to the ground ($D^* = 0.38$; Quinn *et al.* 2014*b*), so there may be cases where it is worth the incurred energy cost to actively maintain an altitude beneath equilibrium. Efficient near-ground swimming would therefore benefit from predictive models of near-ground equilibria. Given that equilibria exist even in inviscid simulations, adapted

added mass and circulatory scalings may be sufficient to model the Strouhal number and reduced frequency dependence observed here. Exploring these equilibria would provide further insight into the behaviour, control and energetics of flatfishes, rays and other near-ground fish or fish-inspired robots.

Acknowledgements

This work was supported by the Office of Naval Research under Program Director Dr R. Brizzolara on MURI grant number N00014-08-1-0642 and BAA grant number N00014-18-1-2537, as well as by the National Science Foundation under Program Director Dr R. Joslin in Fluid Dynamics within CBET on NSF CAREER award number 1653181 and NSF collaboration award number 1921809.

References

BLAKE, R. W. 1983 Mechanics of gliding in birds with special reference to the influence of the ground effect. *J. Biomech.* **16** (8), 649–654.

BLEVINS, E. & LAUDER, G. V. 2013 Swimming near the substrate: a simple robotic model of stingray locomotion. *Bioinspir. Biomim.* **8** (1), 016005.

BRENNEN, C. E. 1982 A review of added mass and fluid inertial forces. *Tech. Rep.* CR 82.010. Naval Civil Engineering Laboratory.

CUI, E. & ZHANG, X. 2010 Ground effect aerodynamics. In *Encyclopedia of Aerospace Engineering*. American Cancer Society.

DAI, L., HE, G. & ZHANG, X. 2016 Self-propelled swimming of a flexible plunging foil near a solid wall. *Bioinspir. Biomim.* **11** (4), 046005.

FERNÁNDEZ-PRATS, R., RASPA, V., THIRIA, B., HUERA-HUARTE, F. & GODOY-DIANA, R. 2015 Large-amplitude undulatory swimming near a wall. *Bioinspir. Biomim.* **10** (1), 016003.

GODOY-DIANA, R., AIDER, J.-L. & WESFREID, J. E. 2008 Transitions in the wake of a flapping foil. *Phys. Rev.* E **77** (1), 016308.

HAINSWORTH, F. R. 1988 Induced drag savings from ground effect and formation flight in brown pelicans. *J. Expl Biol.* **135** (1), 431–444.

IOSILEVSKII, G. 2008 Asymptotic theory of an oscillating wing section in weak ground effect. *Eur. J. Mech. (*B*/Fluids)* **27** (4), 477–490.

KATZ, J. & PLOTKIN, A. 2001 *Low-speed Aerodynamics*, vol. 13. Cambridge University Press.

KEULEGAN, G. H. 1958 Forces on cylinders and plates in an oscillating fluid. *J. Res. Natl Bur. Stand.* **2857**, 423–440.

KIM, B., PARK, S. G., HUANG, W.-X. & SUNG, H. J. 2017 An autonomous flexible propulsor in a quiescent flow. *Intl J. Heat Fluid Flow* **68**, 151–157.

KRASNY, R. 1986 Desingularization of periodic vortex sheet roll-up. *J. Comput. Phys.* **65**, 292–313.

MIVEHCHI, A., DAHL, J. & LICHT, S. 2016 Heaving and pitching oscillating foil propulsion in ground effect. *J. Fluids Struct.* **63**, 174–187.

MOORED, K. W. 2018 Unsteady three-dimensional boundary element method for self-propelled bio-inspired locomotion. *Comput. Fluids* **167**, 324–340.

MOORED, K. W. & QUINN, D. B. 2018 Inviscid scaling laws of a self-propelled pitching airfoil. *AIAA J.* **0** (0), 1–15.

NOWROOZI, B. N., STROTHER, J. A., HORTON, J. M., SUMMERS, A. P. & BRAINERD, E. L. 2009 Whole-body lift and ground effect during pectoral fin locomotion in the northern spearnose poacher (*Agonopsis vulsa*). *Zoology* **112** (5), 393–402.

PAN, Y., DONG, X., ZHU, Q. & YUE, D. K. P. 2012 Boundary-element method for the prediction of performance of flapping foils with leading-edge separation. *J. Fluid Mech.* **698**, 446–467.

PARK, H. & CHOI, H. 2010 Aerodynamic characteristics of flying fish in gliding flight. *J. Expl Biol.* **213** (19), 3269–3279.

PARK, S. G., KIM, B. & SUNG, H. J. 2017 Hydrodynamics of a self-propelled flexible fin near the ground. *Phys. Fluids* **29** (5), 051902.

PERKINS, M., ELLES, D., BADLISSI, G., MIVEHCHI, A., DAHL, J. & LICHT, S. 2018 Rolling and pitching oscillating foil propulsion in ground effect. *Bioinspir. Biomim.* **13**, 016003.

QUINN, D. B., LAUDER, G. V. & SMITS, A. J. 2014*a* Flexible propulsors in ground effect. *Bioinspir. Biomim.* **9** (3), 036008.

QUINN, D. B., MOORED, K. W., DEWEY, P. A. & SMITS, A. J. 2014*b* Unsteady propulsion near a solid boundary. *J. Fluid Mech.* **742**, 152–170.

RAYNER, J. M. V. 1991 On the aerodynamics of animal flight in ground effect. *Phil. Trans. R. Soc. Lond.* B **334** (1269), 119–128.

ROZHDESTVENSKY, K. V. 2006 Wing-in-ground effect vehicles. *Prog. Aerosp. Sci.* **42** (3), 211–283.

TANIDA, Y. 2001 Ground effect in flight. *JSME Intl J. Ser. B Fluids Therm. Engng* **44** (4), 481–486.

VAN TRUONG, T., BYUN, D., KIM, M. J., YOON, K. J. & PARK, H. C. 2013*a* Aerodynamic forces and flow structures of the leading edge vortex on a flapping wing considering ground effect. *Bioinspir. Biomim.* **8** (3), 036007.

VAN TRUONG, T., KIM, J., KIM, M. J., PARK, H. C., YOON, K. J. & BYUN, D. 2013*b* Flow structures around a flapping wing considering ground effect. *Exp. Fluids* **54** (7), 1575.

WEBB, P. W. 1993 The effect of solid and porous channel walls on steady swimming of steelhead trout *Oncorhynchus mykiss*. *J. Expl Biol.* **178** (1), 97–108.

WEBB, P. W. 2002 Kinematics of plaice, *Pleuronectes platessa*, and cod, *Gadus morhua*, swimming near the bottom. *J. Expl Biol.* **205** (14), 2125–2134.

WIE, S. Y., LEE, S. & LEE, D. J. 2009 Potential panel and time-marching free-wake-coupling analysis for helicopter rotor. *J. Aircraft* **46** (3), 1030–1041.

WILLIS, D. J. 2006 An unsteady, accelerated, high order panel method with vortex particle wakes. PhD thesis, Massachusetts Institute of Technology.

ZHANG, C., HUANG, H. & LU, X.-Y. 2017 Free locomotion of a flexible plate near the ground. *Phys. Fluids* **29** (4), 041903.